ChemComm

Chemical Design of Organic Ferroelectrics Using Dynamics of Alkylamide Chains

Journal:	*ChemComm*
Manuscript ID	CC-FEA-07-2022-004120.R2
Article Type:	Feature Article

ARTICLE

Chemical Design of Organic Ferroelectrics Using Dynamics of Alkylamide Chains†

Takashi Takeda and Tomoyuki Akutagawa

Received 00th January 20xx,
Accepted 00th January 20xx

DOI: 10.1039/x0xx00000x

The polypeptide chain is an important structural unit that forms the secondary structure of proteins via intermolecular amide-type N−H•••O= hydrogen bonds. In contrast, alkylamide chains (−CONHC$_n$H$_{2n+1}$) are interesting structural units in which an amide group with a dipole moment and an alkyl chain with high conformational freedom coexist, which have been used to form characteristic molecular assembly structures such as liquid crystals, gels, and supramolecular polymers. One-dimensional chains based on intermolecular N−H•••O= hydrogen-bonding interaction form these molecular assemblies. In the liquid crystal, an electric field – polarization hysteresis curve was observed for alkylamide-substituted benzene derivatives. A molecular design based on the combination of the alkylamide chain, which is the origin of ferroelectricity, and the functional π-electron framework enables the coexistence of ferroelectricity with luminescence, high thermal stability, photoresponse, and current switching properties, and the fabrication of multifunctional molecular materials. The introduction of chiral alkylamide chains is also effective in controlling unidirectional dipole inversion and low coercive electric fields for low-energy-consumption memory devices. Alkylamide chains in molecular assemblies are useful for the development and control of the physical properties of organic ferroelectrics that realize the rotational dynamics of polar amide groups coupled with the melting of alkyl chains in the liquid crystal and solid states.

1. Introduction

The polypeptide chain formed by the condensation of amino acids is an important structural unit that forms secondary protein structures such as α-helix and β-sheet structures with the aid of intermolecular amide-type N−H•••O= hydrogen-bonding interaction.[1,2] Intermolecular N−H•••O= hydrogen bonds of polar amide groups (−CONH−) allow the assembly of polypeptide chains which accumulate and form molecular assemblies by the addition of external energy such as heat. The intermolecular hydrogen-bonding interaction of amide groups have been used in biological molecular assembly structures in vivo because the energy scale of the bond formation and dissociation processes can be controlled at approximately room temperature. Therefore, intermolecular hydrogen bonds between amide groups can be utilized as an important structural unit not only for biomolecules but also for the formation of molecular assembly structures of low-molecular-weight compounds.[3–9]

Alkylamide chains (−CONHC$_n$H$_{2n+1}$) with hydrophobic alkyl groups and polar amide groups are the characteristic structural units in the formation of functional molecular assemblies using intermolecular amide-type N−H•••O= hydrogen bonds. Alkylamide groups are not effective in controlling the electronic structure because their introduction insufficiently changes the highest occupied or lowest unoccupied molecular orbital (HOMO or LUMO) levels of the substituted π-electron system. However, they are important structural units for the formation of organogels and liquid crystal phases, especially in the fabrication of one-dimensional (1D) molecular assemblies. For instance, a discotic columnar liquid crystal phase has been observed in alkylamide-substituted benzene derivatives. Discotic hexagonal columnar (Col$_h$) liquid crystals formed by disc-shaped hydrophobic molecules were first reported by Chandrasekhar in 1977, in which the Col$_h$ liquid crystal phase was observed within a narrow temperature range of 79.4−83.6°C in benzene-derivative bearing hexa –COOC$_8$H$_{17}$ groups. An intermediate mesophase with a molecular aggregate structure is different from a typical calamitic liquid crystal phase exhibited by rod-shaped molecules.[10] The 1D stacking columns of the benzene π-core accompanied by the melting of six lateral alkyl ester chains are arranged in a hexagonal lattice to form a Col$_h$ liquid crystal phase.[11] The very narrow temperature range of the Col$_h$ liquid crystal phase of hexa(alkyl ester)-substituted benzene derivatives is due to weak intermolecular interactions. To overcome this problem, an extended π-system of the central π-core from benzene to hexaphenylbenzene or triphenylene has been used to stabilize the thermal properties of the Col$_h$ phase.[11-13]

A chemical design to significantly improve the thermal stability of the Col$_h$ liquid crystal phase was reported in 1986 by Matsunaga (January 2, 1929–April 2, 2022). *N*,*N*',*N*''-Trialkyl-1,3,5-benzenetricarboxamide (**3BC**) derivatives, in which three alkylamide groups (−CONHC$_n$H$_{2n+1}$) are introduced at the 1, 3, 5-positions of benzene, have been used to form thermally stable

Institute of Multidisciplinary Research for Advanced Materials (IMRAM), Tohoku University, 2-1-1 Katahira, Aoba-ku, Sendai 980-8577, Japan
E-mail: takashi@tohoku.ac.jp and akutagawa@tohoku.ac.jp
† This review is dedicated to Dr. Yoshio Matsunaga (January 2, 1929 – April 2, 2022), Professor Emeritus of Hokkaido University.

Col_h liquid crystal phases over a wide temperature range of 100–200 °C (Fig. 1).[14,15] In addition, *N*,*N*'-Dialkanoyl-2,3,5,6-tetrakis(alkanoyloxy)-1,4-benzenediamine derivatives were obtained to form stable Col_h liquid crystal phases over a wide temperature range of 80–198 °C for n = 10 (Fig. 1).[16] The alkyl ester chains do not form effective intermolecular hydrogen bonds, whereas the alkylamide chains can form multiple 1D N–H•••O= hydrogen bonds to interact with each benzene core along the π-stacking direction. The formation of multiple 1D N–H•••O= hydrogen bonds along the π-stacking columns of benzenes drastically improves the thermal stability of the 1D column structure. Stabilization of the Col_h liquid crystal phase was observed by forming an ordered structure in the temperature region where the hexa(alkyl ester)-substituted benzene derivatives exist in an essentially independent liquid state through intermolecular amide-type N–H•••O= hydrogen bonds. Therefore, alkylamide chains are effective structural units for stabilizing the columnar structures of 1D molecular assemblies. In contrast, hydrogen bonds can increase intermolecular interaction, which also stabilizes the solid phase and results in low solubility in typical organic solvents. The appearance of the Col_h liquid crystal phase of alkylamide-substituted benzene derivatives is governed by several factors, including the number of alkyl chains relative to the π-electron core of benzene, the position of substitution, and the magnitude of the π-π interaction, because the lateral alkyl chains are completely in a melting state similar to the liquid state. With regards to alkylamide-substituted benzene derivatives, the appearance of Col_h and discotic nematic (N_D) liquid crystal phases on introduction of multiple –$CONHC_nH_{2n+1}$ chains has been reported in various benzene derivatives such as toluene, xylene, mesitylene, and tetramethylbenzene derivatives.[17–22] The intermolecular amide-type N–H•••O= hydrogen-bonding interaction is effective for the design of 1D molecular assembly structures (Fig. 1b).

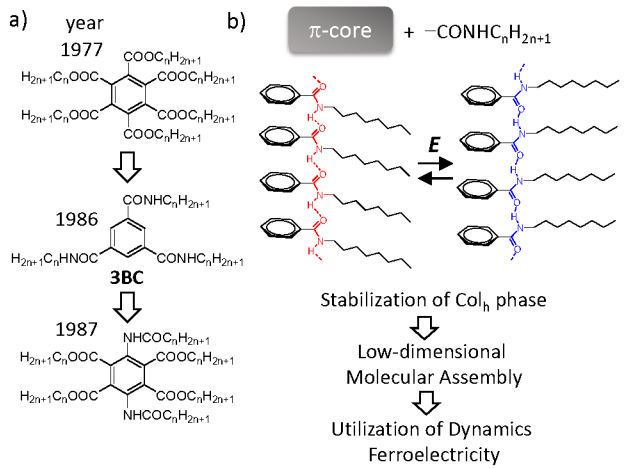

Fig. 1. Design of Col_h liquid crystalline phases and functional organic materials utilizing alkylamide chains. a) Formation of intermolecular amide-type N–H•••O= hydrogen bonds and stabilization of Col_h liquid crystalline phases. b) Design of π-cores and introduction of alkylamide chains for the formation of low-dimensional molecular assemblies and organic ferroelectrics utilizing inversion dynamics of polar amide groups.

Alkylamide chains are also an effective substituent for the formation of organogels.[19–21] Organogels are binary molecular assemblies in which amphiphilic molecules form 1D fibrous molecular assemblies that entangle three-dimensional (3D) higher-ordered molecular assemblies with pores, in which solvent molecules include and remain.[23–25] By the incorporation of solvent molecules such as toluene, chloroform, and ethanol into pores formed by 3D entanglement assembly structures of each fiber, the physical organogels of **3BC** were fabricated by intermolecular amide-type N–H•••O= hydrogen-bonding interaction.[26,27] The absence of organogel formation in hexa(alkyl ester)-substituted benzene derivatives is associated with weak intermolecular interactions, suggesting an important structural unit of alkylamide chains for organogel formation. By controlling the alkyl chain length, it is possible to adjust the Col_h liquid crystal phase and organogelation ability. The formation of 1D molecular assemblies by the aid of intermolecular amide-type N–H•••O= hydrogen-bonding interaction was confirmed by X-ray diffraction patterns by Malthête et al. in 1992.[28] In addition, Meijer et al. considered 1D hydrogen-bonded molecular assemblies as supramolecular polymers and conducted a series of studies on the control of their arrangement.[30–45] For instance, helical columnar structures using chiral alkylamide-substituted benzene derivatives have been reported as interesting chiral 1D self-assembly processes such as the Sergeants-and-Soldiers effect and chiral amplification by addition of a small amount of chiral molecule into an achiral one.[39,40] Further extension of the fabrication of functional nanofibers based on hydrogen-bonding interactions of alkylamide chains to functional π-electron cores are capable of electrical conducting and luminescent properties.[41, 42] Sugiyasu et al. have studied 1D supramolecular polymers formed by alkylamide-substituted porphyrin derivatives on substrate surface by means of a nuclear growth model.[43-45] Miyashita et al. reported that alkylamide-substituted polymers form stable hydrogen-bonded Langmuir-Blodgett films at the air-water interface, and have fabricated stable free-standing molecular films using the formation of a two-dimensional (2D) hydrogen-bonding network of amide groups as a driving force.[46,47]

Organic ferroelectrics based on various polarization inversion mechanisms such as intermolecular hydrogen bonding, charge transfer, molecular rotation, dynamics in liquid crystalline state, fluorinated polymer, etc have been developed and their application to memory devices has attracted much attention.[48-57] In typical solid-state ferroelectrics, the real part dielectric constant (ε_1) shows a peak independent of the measured frequency at the phase transition temperature (T_c) from the high-temperature paraelectric phase to the low-temperature ferroelectric phase (Scheme 1a). In the low-temperature ferroelectric phase, the *P*-*E* curve shows hysteresis, and coercive electric filed (E_t), saturated polarization (P_s), and remanent polarization (P_r) are representative physical parameters for ferroelectric responses (Scheme 1b). The large P_r value at E=0 is important from the viewpoint of memory device applications, and the small E_t is essential for the low energy switching. The shape of the *P*-*E* hysteresis is governed by the magnitude of the

leakage current, the dimensionality, and crystallinity of the ferroelectric material.

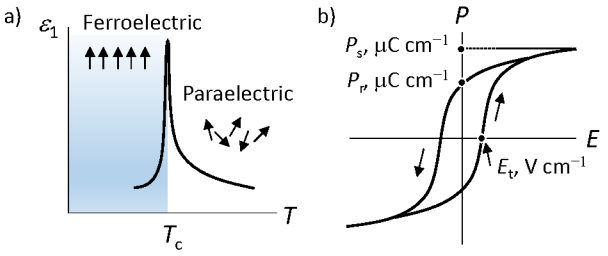

Scheme 1. Ferroelectricity phase transition and physical aspect of solid state. a) Temperature dependent real part dielectric constants (ε_1). Sharp ε_1 peak at high temperature paraelectric phase to low temperature ferroelectric phase. b) Ferroelectric *P*-*E* hysteresis curve. Coercive electric filed (E_t), saturated polarization (P_s), and remanent polarization (P_r) are important physical parameter for ferroelectric response.

In the Col_h liquid crystal phase of **3BC** derivatives, Sjebelma et al. reported that the application of an electric field (*E*) induces a hysteresis loop in the electric field polarization (*P*-*E*) curve, which is characteristic of ferroelectrics.[58-62] The alkyl chains of **3BC** are in a liquid-like melting state. Recently, various functional π-system with amide units have been designed and reported with respect to the control of molecular assembly structures and the development of ferroelectricity.[63,64] The usefulness of amide type hydrogen-bonding interaction for controlling the assembly structures and physical properties has been demonstrated, and their applications are being actively investigated.

Macroscopic polarization of a columnar structure is generated by intermolecular amide-type N–H•••O= hydrogen bonds along the direction parallel to the polarized column, where the direction of intermolecular hydrogen bonds concertedly inverts from N–H•••O= to =O•••H–N. The design of the alkyl chain length can adjust the inversion energy of the hydrogen bonds and *P*-*E* hysteresis curve. The ferroelectricity of the Col_h liquid crystal phase differs from that of the ferroelectric-paraelectric phase transition of bulk solids. The polarization inversion state in the liquid crystal state is affected by the thermal fluctuations of the alkyl chains, and the relaxation of the polarization state is faster than that in the solid state. Furthermore, the frequency (*f*)- and temperature (*T*)-dependent real part of the dielectric constant (ε_1) does not show a clear ε_1 peak around the solid to ferroelectric phase transition temperature.[65] The low-*T* phase of bulk solid-state ferroelectrics is a dipole-ordering electric ground state with broken symmetry, whereas the high-*T* phase is a paraelectric phase with thermally fluctuating dipole moments. The state changes of these two are classified into the atomic displacement type and order-disorder type. In the case of liquid crystalline ferroelectrics, a phase transition to a paraelectric isotropic liquid occurs in the transition from the ferroelectric state upon further temperature increase, and the behaviour of the *T*-change in the dielectric constant differs from that in bulk ferroelectric solids. In this review, we introduce our recent research on the phase transition behaviour, molecular assembly structure, ferroelectricity, and multifunctionality of π-conjugated molecules with substituted alkylamide chains in various functional π-electronic cores.

2. Ferroelectricity of liquid crystalline alkylamide-substituted benzene derivatives

There are various hydrogen-bonding modes, such as O–H•••O and N–H•••N. Among them, the amide-type N–H•••O= hydrogen-bonding interactions have a moderate energy scale and dipole moment, and can be utilized for a polarization inversion unit in which the direction of hydrogen-bonding interaction can be reversibly controlled by the application of an external electric field *E*. However, it is difficult to invert the N–H•••O= hydrogen-bonding direction by application of *E* in the closest-packing structures of static crystals. In contrast, inversion of alkylamide chains is easily achieved in thermally fluctuating molecular assemblies such as liquid crystalline phases. The inversion of the amide group in 1D N–H•••O= hydrogen-bonded chains occurs during macroscopic dipole inversion. Liquid crystalline alkylamide-substituted benzene derivatives are an ideal molecular systems for realizing ferroelectric polarization inversion dynamics because they can construct thermally fluctuating 1D amide-type hydrogen-bonding chains. Even if a π-electron core is used instead of simple benzene, the introduction of an alkylamide chain can form a Col_h liquid crystal phase with a 1D amide-type N–H•••O= hydrogen-bonded chain.

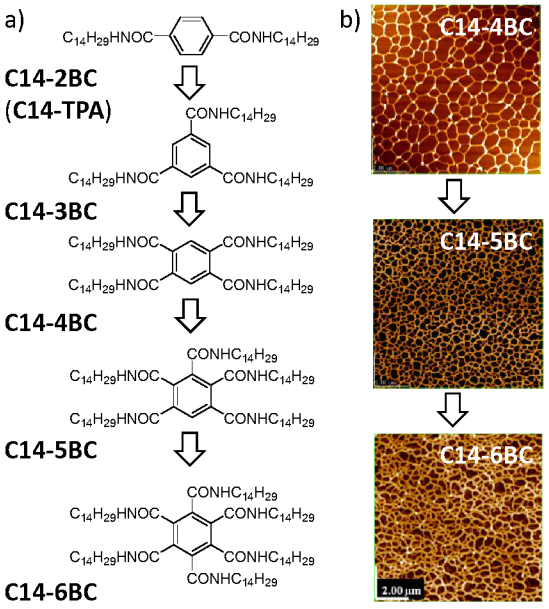

Fig. 2. Molecular structures of a) **C14-2BC** (**C14-TPA**), **C14-3BC**, **C14-4BC**, **C14-5BC**, and **C14-6BC** with introduction of diverse $-CONHC_{14}H_{29}$ chains and b) spiderweb-like nanowire network structures formed by **C14-4BC**, **C14-5BC**, and **C14-6BC** on mica substrate surface (scale bar 2 μm). Adapted with permission from ref. 66. Copyright 2014 American Chemical Society.

The number of alkylamide chains and its position of substitution are important for the presence of ferroelectricity in

alkylamide-substituted benzene derivatives; we investigated the relationship between chemical structures and physical properties (Fig. 2a).[66] Fixed-length alkylamide chains of $-CONHC_{14}H_{29}$ are introduced into various substituted positions of benzene and the molecular assembly structure and ferroelectricity of each derivative are investigated. With the exception of the para-substituted benzene derivative of **C14-2BC** (**C14-TPA**), tri-chain **C14-3BC**, tetra-chain **C14-4BC**, penta-chain **C14-5BC**, and hexa-chain **C14-6BC** derivatives with three to six alkylamide chains form a Col_h liquid crystal phase with increasing temperature, and effective intermolecular N−H•••O= hydrogen-bonding interactions are observed in the formation of a 1D columnar structure. Spin-coated films of **C14-3BC**, **C14-4BC**, **C14-5BC**, and **C14-6BC** on mica substrates show the formation of a higher-order molecular assembly structure with spiderweb-like nanowire molecular aggregates with a diameter of ~20 nm and a height of 2 nm (Fig. 2b). The occupation density of the web-like fiber structure on the substrate surface increases with the number of alkylamide chains, and the occupation of the fiber network on the substrate surface structure increases in the order of **C14-6BC** > **14-5BC** > **C14-4BC** > **C14-3BC**. The number of amide units involved in intermolecular hydrogen-bonding interaction plays an important role in the formation and strength of molecular assembly structures. Furthermore, **C14-3BC**, **C14-4BC**, **C14-5BC**, and **C14-6BC** form organogels in various organic solvents such as toluene, chloroform, and ethanol, confirming the existence of 1D fibrous molecular assembly structures through intermolecular N−H•••O= hydrogen-bonding interaction.

Benzene derivatives of **C14-3BC**, **C14-4BC**, **C14-5BC**, and **C14-6BC** with three or more $-CONHC_{14}H_{29}$ chains exhibited the Col_h liquid crystal phase; however, ferroelectricity was observed only in **C14-3BC** and **C14-5BC** (Fig. 3a). The ferroelectricity of the two-chain system **C14-2BC** (**C14-TPA**) is discussed in a later section. Interestingly, ferroelectricity was not observed in **C14-4BC** or **C14-6BC** with high molecular symmetry, indicating that the molecular structure was correlated with the appearance of ferroelectricity. Ferroelectricity was confirmed by observing the *P*-*E* hysteresis curves using liquid crystal electrode cells with micrometer gaps, and hysteresis was observed in the Col_h liquid crystal phase for **C14-3BC** and **C14-5BC** (Fig. 3a). The presence of leakage current may obscure the *P*-*E* hysteresis curve, while the appearance of a butterfly-shaped curve in the d*P*/d*E* - *E* plot confirms the presence of P_r and E_t values (upper in Fig. 3a). Differences in the *T*- and *f*-dependent dielectric constants were observed between the ferroelectric **C14-3BC** (**C14-5BC**) and antiferroelectric **C14-4BC** (**C14-6BC**). In the latter molecular system, the *f*-response of the real part of dielectric constant ε_1 had a small magnitude without drastic dielectric enhancement (Fig. 3c). The motional freedom of the polar amide units responsible for *E* is a different environment for the two systems. The polar amide groups of ferroelectric **C14-3BC** and **C14-5BC** are sufficiently responsible for the application of *E*, whereas the degrees of motional freedom for non-ferroelectric **C14-4BC** and **C14-6BC** are considered to be low. The more symmetrical **C14-4BC** and **C14-6BC** molecules allow the formation of effective intra- and inter-molecular N−H•••O= hydrogen-bonded 1D columns (Fig. 3d), reducing the degree of motional freedom of the polar structural units relative to the application of *E*. The introduction of an alkylamide chain at the nearest neighboring-adjacent position of benzene results in the formation of an effective intramolecular hydrogen-bonding structure, and steric hindrance prevents the dipole inversion of the amide group. The broken molecular symmetry of the lower-symmetry **C14-5BC** does not contribute to the intramolecular hydrogen-bonding interaction, and remains a frustrated hydrogen-bonding unit. As a result, a macroscopic dipole moment was observed in the dipole inversion phenomena. The study of the various substitution positions and number of alkylamide chains for the benzene π-core clarified the requirements for the molecular structural condition for the presence of ferroelectricity and enabled further molecular design to realize multifunctional molecular materials.

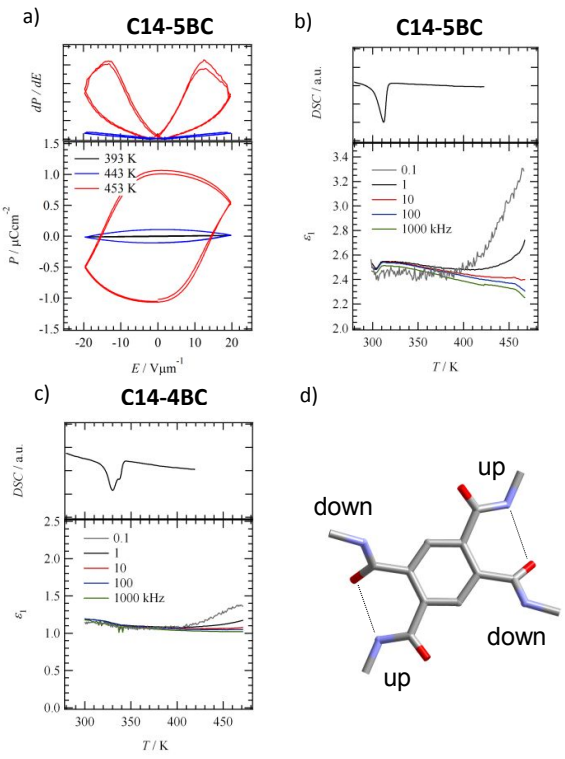

Fig. 3. Dielectric properties of $-CONHC_{14}H_{29}$ substituted benzene derivatives. a) *T*-dependent *P*-*E* curves at *f* = 1.0 Hz and derivative of polarization values (d*P*/d*E*)−*E* plots for **C14-5BC**. b, c) *T*- and *f*-dependent real part dielectric constants (ε_1) of b) **C14-5BC** and c) **C14-4BC** with the solid-Col_h liquid crystal phase transition behaviour based on the DSC charts. d) Intramolecular N−H•••O= hydrogen-bonding structure of **C14-4BC**. Adapted with permission from ref. 66. Copyright 2014 American Chemical Society.

3. Extension of π-electronic system to design additional functions

A wide variety of π-molecules are candidates for the introduction of alkylamide chains into π-electronic systems. For example, excellent luminescent pyrene, porphyrins with characteristic absorption bands, and azobenzene with photoisomerization

reactions are candidates for the fabrication of multifunctional ferroelectrics. First, we investigated the liquid crystallinity and ferroelectricity of the pyrene derivative (**4Py**), in which four alkylamide chains (−CONHC$_{14}$H$_{29}$) were introduced into the fluorescent π-core, which is known to exhibit excellent optical properties (Fig. 4a).[67] **4Py** formed a Col$_h$ liquid crystal phase at *T*-range of 295−450 K from polarized optical microscope (POM), X-ray diffraction (XRD), and differential scanning calorimetry (DSC) measurements and organogels with green and fluorescent response in toluene and chloroform (Fig. 4b). The concentration-dependent absorption-emission spectra in chloroform showed a change from monomer (blue) to excimer (green) emission with increasing concentration similar to pyrene (Fig. 4c). Interestingly, conversion from monomer to excimer emission was observed at a low concentration of 10^{-6} M, three orders of magnitude lower than that of unsubstituted pyrene. **4Py** molecules form stable 1D molecular assemblies with the aid of intermolecular N−H•••O= hydrogen-bonding interaction at concentrations as low as 10^{-6} M in chloroform.

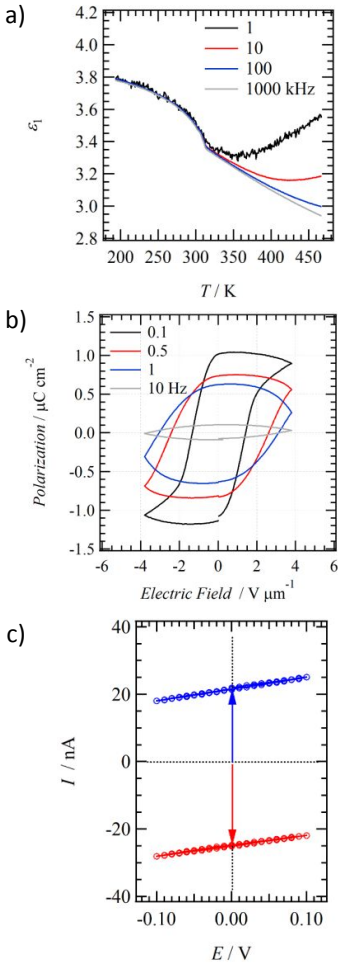

Fig. 4. Alkylamide-substituted pyrene derivative of **4Py**. a) Molecular structure of **4Py**. b) Photographs of organogels formed by **4Py** in chloroform under normal light (left) and UV irradiation (right). c) Concentration-dependent absorption (left scale) and emission spectra (right scale) of **4Py** in chloroform. Adapted with permission from ref. 67. Copyright 2015 American Chemical Society.

The *T*- and *f*-dependent real part of dielectric constant ε_1 shows a slight anomaly near the phase transition temperature from the solid to the Col$_h$ liquid crystal phase. In general, an ε_1 peak accompanying the transition to ferroelectricity has been observed in bulk ferroelectrics, whereas such behaviour has not been observed in the phase transition to the isotropic liquid state (Fig. 5a). The *P*-*E* curve of the Col$_h$ liquid crystalline phase at 390 K for the measurement *f*-range of 0.1–1.0 Hz shows hysteresis behaviour by dipole inversion, indicating the presence of ferroelectricity in the Col$_h$ liquid crystal phase similar to that of **C14-3BC**. The remanent polarization (P_r) and coercive electric field (E_t) at 490 K for f = 1.0 Hz are 1.0 μC cm^{-2} and 1.5 V μm^{-1}, respectively (Fig. 5b).

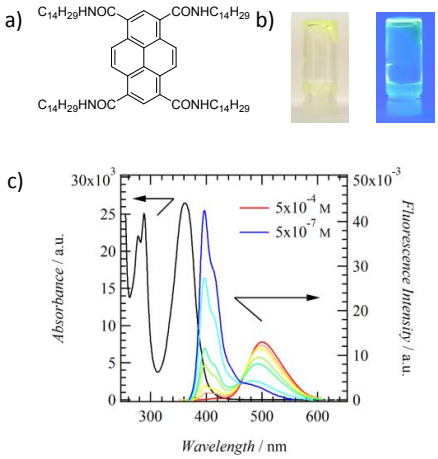

Fig. 5. Electrical properties of **4Py**. a) *T*- and *f*-dependent real part of dielectric constant ε_1. b) *f*-dependent *P*-*E* curve at 490 K. c) *I*-*V* characteristics after orientation of ferroelectric polarization. Blue and red curves are measured after orientation of polarization by application of +10 V and −10 V pulse voltage. Adapted with permission from ref. 67. Copyright 2015 American Chemical Society.

The introduction of the −CONHC$_{14}$H$_{29}$ chain into the pyrene π-core allowed the formation of a ferroelectric response with additional fluorescent properties. Interestingly, **4Py** exhibited a current-switching phenomenon that depended on the ferroelectric polarization history. When the current-voltage (*I*-*V*) characteristics were measured after the ferroelectric polarization was aligned in the positive direction by applying a +10 V pulse voltage, the linear *I*-*V* characteristics according to Ohm's law were shifted to the positive current direction (Fig. 5c). This is because of the ferroelectric polarization that generates an internal voltage E_{loc} at V = 0 V. Since the current zero voltage was observed at −0.6 V, the E_{loc} value in **4Py** ferroelectric molecular assembly was estimated to be ~0.6 V. Furthermore, when a pulse voltage of −10 V was applied in the opposite direction to align the ferroelectric polarization direction to the negative direction, the *I*-*V* characteristic with a bias in the negative current direction was confirmed. Thus, a current-switching phenomenon of the *I*-*V* characteristics was observed in the *P*-*E* hysteresis of the ferroelectric polarization. Despite the simple pyrene derivative, the introduction of alkylamide chains has revealed a wide variety of molecular assembly structures and physical properties, including ferroelectricity, fluorescence properties, current

switching phenomena, nanowires, liquid crystallinity, organogel formation, and low-concentration excimer emission.

Based on the ferroelectricity of **4Py**, we synthesized a porphyrin derivative of **4Por** with four −CONHC$_{14}$H$_{29}$ chains for the tetrabenzoporphyrin π-core and attempted to study its molecular assembly structure, phase transition behaviour, and ferroelectricity (Fig. 6a).[68] Because of the expansion of the π-electron core, the formation of a discotic columnar liquid crystal phase was confirmed in a wide *T*-range of 444–564 K (Fig. 6b), which was assigned to a discotic rectangular columnar (Col$_r$) liquid crystal phase from *T*-variable XRD patterns. Typical optical absorptions of Soret-band at 420 nm and Q-bands at 516, 551, 591, and 646 nm, characteristic of the porphyrin π-core, were observed. The *T*- and *f*-dependent real part of dielectric constant ε_1 showed an increase in response to the low-*f* condition in the *T*-range above 460 K, similar to benzene derivatives such as **C14-3BC**, indicating that the thermal motion of the polar amide-type N−H•••O= hydrogen bonds is activated in the Col$_r$ liquid crystal phase. The *P*-*E* curve at 503 K showed a hysteresis behaviour of ferroelectrics, with P_r and E_t values of ~1 μC cm^{-2} and 1 V μm^{-1} at f = 0.1 Hz, respectively (Fig. 6c). The observation of ferroelectric hysteresis in thermally stable **4Por** even in the high-*T* region above 500 K suggests the design of nonvolatile memory that can operate under high-*T* conditions.

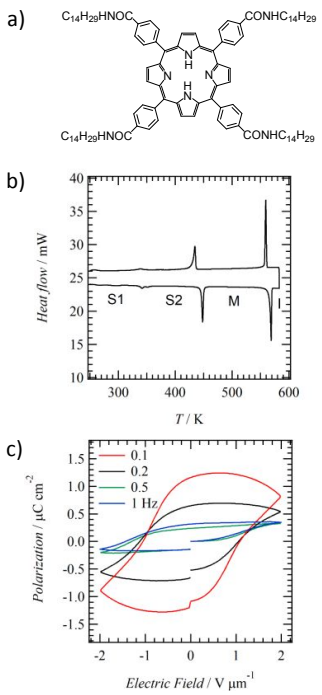

Fig. 6. Liquid crystallinity and ferroelectricity of **4Por**. a) Molecular structure of **4Por** and b) phase transition behaviour based on DSC charts. c) *f*-dependent *P*-*E* hysteresis curve at 510 K. Adapted with permission from ref. 68. Copyright 2019 American Chemical Society.

We focused on azobenzene (**Az**) derivatives known for photo-induced *cis*-*trans* isomerization system, synthesizing three molecules with −CONHC$_{10}$H$_{21}$ chains (**Az-1**, **Az-2**, and **Az-3**) and investigating their liquid crystalline properties, molecular assembly structures, and ferroelectric properties (Fig. 7a).[69] **Az** derivatives with rod-shaped molecular structures are considered to form a calamitic liquid crystal phase rather than a columnar one. The three Az derivatives – **Az-1** having only one −CONHC$_{10}$H$_{21}$ chain, **Az-2** having a decyl chain (−C$_{10}$H$_{21}$) and a −CONHC$_{10}$H$_{21}$ chain, and **Az-3** having two −CONHC$_{10}$H$_{21}$ chains – were designed to compare their molecular assembly and ferroelectricity. The **Az-2** and **Az-3** derivatives showed ferroelectric *P*-*E* hysteresis behaviour.

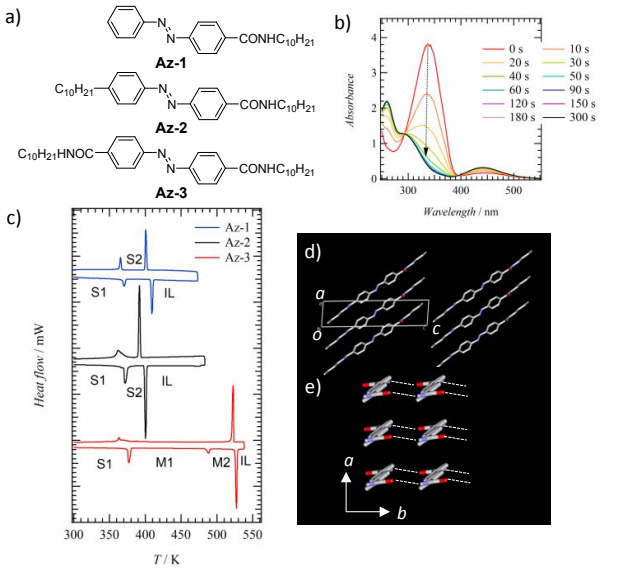

Fig. 7. Alkylamide-substituted azobenzene derivatives. a) Molecular structures of **Az-1**, **Az-2**, and **Az-3** and b) *trans*-to-*cis* isomerization of **Az-3** in DMF by photoirradiation (365 nm). c) DSC curves and phase transition behaviour of **Az-1**, **Az-2**, and **Az-3**. d) Unit cell viewed along the *b*-axis and e) double 1D N−H•••O= hydrogen-bonding chains determined by single-crystal X-ray structural analysis of **Az-3** derivative with −C$_4$H$_9$ chains (CCDC-2084963 and 2084964). Adapted with permission from ref. 69. Copyright 2021 American Chemical Society.

The *cis*-*trans* isomerization of these **Az** derivatives was examined by photoirradiation at 365 nm in the solution phase, and it was confirmed that the *trans*-*cis* isomerization reaction occurred in 80% yield in dimethylformamide (DMF) after ~1 min of photoirradiation (Fig. 7b). Phase transition behaviour based on DSC charts revealed only the solid-solid phase transition for **Az-1** and **Az-2**, while solid-M1 and M1-M2 phase transitions were observed for **Az-3**, indicating the existence of intermediate liquid crystal M1 and M2 phases (Fig. 7c). **Az-3** with two decylamide chains indicates two different liquid crystalline phases, M1 and M2, as *T* increases. *T*-variable powder XRD measurements confirmed the formation of lamellar-type liquid crystal phases of M1 and M2, in which double 1D N−H•••O= intermolecular hydrogen-bonding interactions at two −CONHC$_{10}$H$_{21}$ chains connected each rod-like molecule. Single-crystal X-ray structure analysis of **Az-3** derivative with butyl chains confirmed the formation of double 1D N−H•••O= intermolecular hydrogen bonds between the two terminal alkylamide chains at **Az-3** (Figs. 7d, e). The formation of a similar molecular assembly structure was also confirmed in **Az-3**, suggesting that the two −CONHC$_{10}$H$_{21}$ chains were thermally melted upon increasing *T* in the liquid crystalline phase. The

melting of the alkyl chains contributed significantly to the polarization inversion of the hydrogen-bonding N–H•••O= groups.

The *T*- and *f*-dependent real part of dielectric constant ε_1 of **Az-3** increased slightly with the phase transition from the solid to the lamellar M1 liquid crystal phase, and a large dielectric ε_1 response was observed at much lower *f* conditions (Fig. 8a). *P*-*E* curves in the solid-state high-*T* phase (S2) of **Az-2** and the lamellar liquid crystal phases (M1 and M2) of **Az-3** showed ferroelectric *P*-*E* hysteresis curves, and the presence of a butterfly-shaped $\Delta P/\Delta E$ - *E* plot also corresponds to the presence of a clear E_t value (upper in Fig. 8a). The P_r and E_t values of **Az-3** at 473 K with $f = 0.1$ Hz were 4.35 μC cm^{-2} and 14.6 V μm^{-1}, respectively, while those of **Az-2** at 395 K with $f = 0.1$ Hz were 2.11 μC cm^{-2} and 15.7 V μm^{-1}. Interestingly, ferroelectricity was observed in the solid-state S2-phase of **Az-2**, which did not exhibit a liquid crystal phase. In contrast, the ferroelectric *P*-*E* curve was not observed in the measured *T*-region of **Az-1**. The inversion dynamics of the amide group requires assistance from the melting of the alkyl chain. Therefore, sufficient thermal motion in **Az-1** was not activated in the high-*T* solid phase. Ferroelectricity can also be achieved in –CONHC$_{10}$H$_{21}$ substituted **Az** derivatives with a lamellar-type double 1D N–H•••O= hydrogen-bonding molecular configuration. The introduction of alkylamide chains is an effective chemical approach for designing ferroelectricity for the liquid crystalline state of a wide range of π-molecules with disc- and rod-shaped molecules. However, the photoirradiation effect in the lamellar liquid crystal phase of **Az-3** resulted in insufficient structural isomerization from the *trans*- to *cis*-configuration. The dielectric constant and *P*-*E* hysteresis curves show no change after photoirradiation, suggesting that it is difficult to induce the dynamics of structural isomerization by photoirradiation in the liquid crystalline phase.

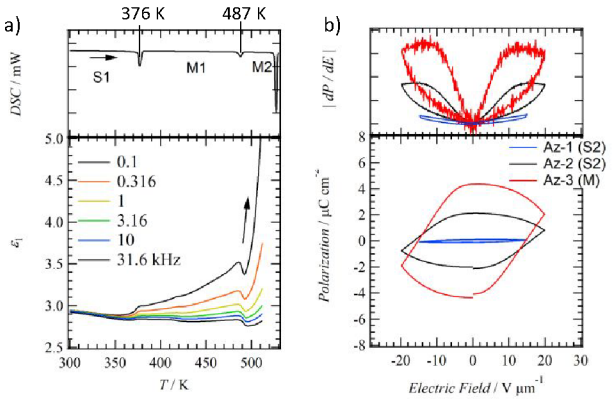

Fig. 8. Dielectric properties of alkylamide-substituted azobenzene derivatives. a) *T*- and *f*- dependent real part of dielectric constant ε_1 of **Az-3** and its DSC chart in the heating process. b) *P*-*E* curves at $f = 0.1$ Hz and (d*P*/d*E*)–*E* plots of **Az-1** (S2 phase), **Az-2** (S2 phase), and **Az-3** (M phase). Adapted with permission from ref. 69. Copyright 2021 American Chemical Society.

The intermolecular amide-type N–H•••O= hydrogen-bonding interaction plays an effective role in the fabrication of ferroelectric molecular assembly structures based on the design of π-electron cores in either disc-shaped or rod-shaped molecules, where the inversion motion of polar structural units can be used for ferroelectricity.

We synthesized a dimethyl[4]helicene derivative in which two –CONHC$_{14}$H$_{29}$ chains are introduced into a non-planar π-electron core of dimethyl[4]helicene, and attempted to study its molecular assembly structure, phase transition behaviour, dielectric response, and ferroelectricity (Fig. 9a).[70] Dimethyl[4]helicene bearing two –CONHC$_{14}$H$_{29}$ chains (**Hel**) is a chiral molecule that retains its helicated conformation at room temperature due to steric repulsion of the methyl groups. Interestingly, the molecular assembly structure and phase transition behaviour of racemic *rac*-**Hel** and chiral (*P*)-**Hel** are significantly different. The phase transition from the solid to the liquid crystal phase was observed only in *rac*-**Hel** at 330 K with increasing *T*, and the phase transition from the liquid crystal to the isotropic liquid phase appeared at 420 K (Fig. 9b).

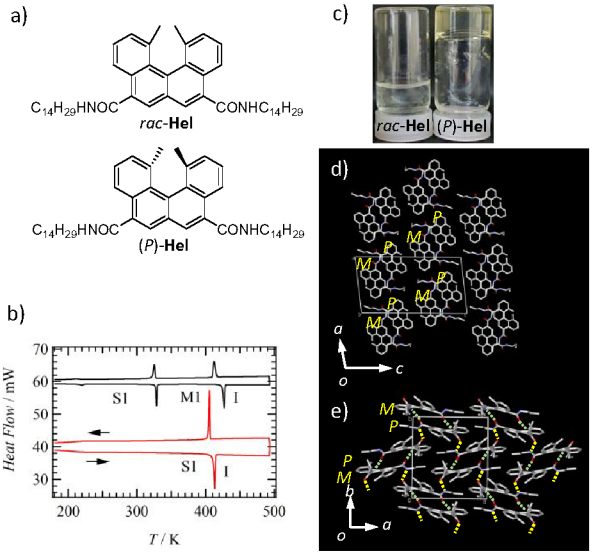

Fig. 9. a) Molecular structure of *rac*-**Hel** and (*P*)-**Hel**. b) Phase transition behaviour by DSC charts (black: *rac*-**Hel** and red: (*P*)-**Hel**). c) Difference in organogelation ability in chloroform-hexane. d) Single-crystal X-ray structural analysis of *rac*-**Hel** with –CONHC$_3$H$_7$ chains (CCDC-1873930). Unit cell viewed along the *b*-axis e) *P*-*M* dimer formation and 2D hydrogen-bonding layers in the *ab*-plane. Adapted with permission from ref. 70. Copyright 2019 American Chemical Society.

In contrast, (*P*)-**Hel** did not show liquid crystallinity, and only a phase transition from the solid to the liquid phase was observed at 400 K. A clear difference was also observed in organogelation ability. (*P*)-**Hel** became an organogelator, whereas *rac*-**Hel** did not form an organogel (Fig. 9c). Therefore, the molecular assembly structures of the *rac*-**Hel** and (*P*)-**Hel** forms are different. Single-crystal X-ray structural analysis of *rac*-**Hel** with a propylamide chain (–CONHC$_3$H$_7$) revealed the formation of N–H•••O= hydrogen-bonded *P*-*M* dimers arranged in 2D in the *ab*-plane, forming amide-type hydrogen-bonding layers in the *ab*-plane (Figs. 9d, e). These 2D hydrogen-bonded layers are aligned along the *c*-axis to form a lamellar structure. The difference in organogelation ability is associated with the dimensional difference in the molecular assemblies, where (*P*)-

Hel and *rac*-**Hel** form 1D and 2D molecular assemblies, respectively.

The *T*- and *f*-dependent real part of dielectric constant ε_1 was evaluated using *rac*-**Hel**, which exhibited a lamellar liquid crystal phase, and a sharp ε_1 increase in the low-*f* region was observed as the *T* increased after phase transition to the liquid crystal phase (Fig. 10a). The *P*-*E* curves were measured in the *T*-range of 343−423 K, and the *P*-*E* hysteresis behaviour was confirmed in the *T*-range where the ε_1 enhancement at low-*f* was significant (Fig. 10b). P_r and E_t values of *rac*-**Hel** at $f = 0.5$ Hz are 2.5 μC cm^{-2} and 22 V μm^{-1}, respectively, which are larger than these values for **C14-3BC** and **4Py**. The formation of 2D intermolecular amide-type N−H•••O= hydrogen bonds increases the outer energy required for polarization inversion, resulting in a larger value of E_t. Furthermore, unlike 1D assembly structures, polarization domains can be aligned in 2D structures without any poling treatment, which may be related to the enhancement of P_r value. Controlling the dimensionality of intermolecular hydrogen-bonding structures is an effective chemical technique for designing ferroelectric parameters such as P_r and E_t values.

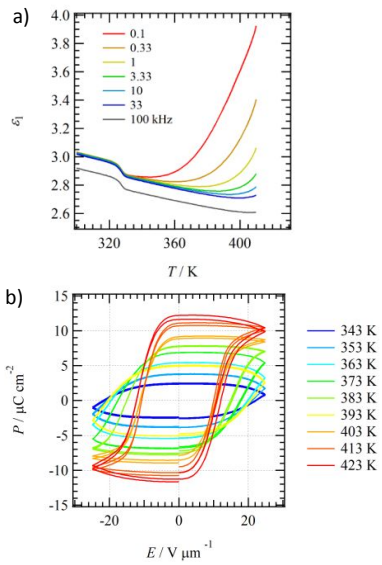

Fig. 10. Dielectric and ferroelectric behaviour of *rac*-**Hel**. a) *T*- and *f*-dependent real part of dielectric constant ε_1 and b) *T*-dependent *P*-*E* curves at $f = 0.5$ Hz. Adapted with permission from ref. 70. Copyright 2019 American Chemical Society.

4. Formation of mixed crystals and control of ferroelectric property

The physical properties of liquid-crystalline ferroelectrics are significantly affected by the formation of mixed crystals. In general, the same type of liquid crystalline phase can be mixed, and this phenomenon has been utilized to identify unknown liquid crystalline phases. While the formation of a mixture in the solid state is known to be limited by the same space groups and molecular geometries, the formation of a mixture is relatively easy in the liquid crystalline phase. We have previously reported that ferroelectric **C14-3BC** and antiferroelectric **C14-4BC** can form the same Col$_h$ liquid crystal phase.[71] The molecular assembly structure and ferroelectricity change when ferroelectric **C14-3BC** and antiferroelectric **C14-4BC** are mixed together (Fig. 11a).[57] The doping of antiferroelectric **C14-4BC** into a 1D column of ferroelectric **C14-3BC** is expected to have a significant effect on the ferroelectric properties originating from N−H•••O= hydrogen bonding inversion.

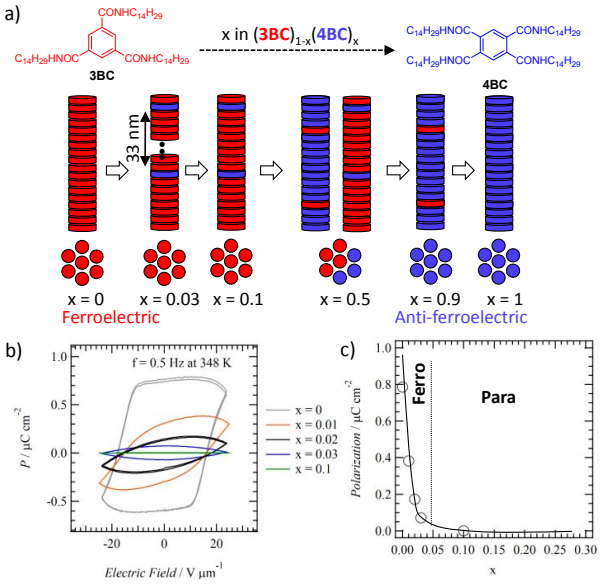

Fig. 11. Control of ferroelectric properties by the formation of mixed crystal (**C14-3BC**)$_{1-x}$(**C14-4BC**)$_x$ of ferroelectric **C14-3BC** and antiferroelectric **C14-4BC**. a) Schematic of mixed state of **C14-3BC** (red) and **C14-4BC** (blue). b) *P*-*E* hysteresis curve for mixing rate x at $f = 0.5$ Hz and $T = 348$ K. c) x-dependent P_r value and abrupt drop from ferroelectric to paraelectric states. Adapted with permission from ref. 71. Copyright 2020 American Chemical Society.

The **C14-3BC** and **C14-4BC** molecules may be randomly mixed in a 1D column; each **C14-3BC** and **C14-4BC** column may be separated in a domain or may be mixed. When antiferroelectric **C14-4BC** was randomly mixed into the ferroelectric **C14-3BC** column, one **C14-4BC** molecule was introduced into 100 molecules of **C14-3BC** for a 1% doping ratio and ten **C14-4BC** molecules were introduced into 100 molecules of **C14-3BC** for a 10% doping ratio. When more than 10% **C14-4BC** was doped into **C14-3BC**, low-angle (100) reflection peaks of the Col$_h$ phases of **C14-3BC** and **C14-4BC** were observed independently, indicating a domain separation state. Therefore, **C14-3BC** and **C14-4BC** cannot freely mix with each other. In contrast, when the doping ratio of **C14-4BC** was lower than 10%, the domain structure of **C14-3BC** was retained, and the antiferroelectric **C14-4BC** was randomly introduced into the ferroelectric **C14-3BC** 1D column. We studied the effect of **C14-4BC** doping on the ferroelectricity of **C14-3BC** columns at low **C14-4BC** doping rates of less than 10%. As the doping rate of **C14-4BC** relative to **C14-3BC** increased from 0 to 10%, the *T*- and *f*-dependent dielectric response ε_1 under the low-*f* condition was gradually suppressed in the presence of **C14-4BC**. Polarization inversion of the amide group of **C14-3BC** was restricted by the presence of **C14-4BC**. Therefore, antiferroelectric **C14-4BC** acted as a pinning potential for the polarization inversion of the

ferroelectric 1D column. *P*-*E* curves measured at f = 5.0 Hz and T = 348 K for 1, 2, 3, and 10% doping mixtures of **C14-4BC** show significant suppression of P_r values with increasing **C14-4BC** doping ratio (Fig. 11b). The P_r value of 0.8 μC cm^{-2} for **C14-3BC** halved to 0.4 μC cm^{-2} by doping only 1% **C14-4BC**, decreased to 0.2 μC cm^{-2} by doping 2%, and remained the same by doping 3% (Fig. 11b). The presence of 3% **C14-4BC** corresponds to the random introduction of three molecules of **C14-4BC** for every 100 molecules of 1D column of **C14-3BC**, assuming a π-stack distance of 0.37 nm. Therefore, 1 and 10% doping of **C14-4BC** corresponded to ferroelectric **C14-3BC** column lengths of 37 and 3.7 nm, respectively, and 3% doping of **C14-3BC** corresponded to a 1D column length of approximately 10 nm. A minimum correlation length of ~10 nm is required to maintain a ferroelectric 1D column correlation length by dipole inversion. A doping of a small amount of **C14-4BC** into ferroelectric **C14-3BC** hydrogen-bonding column suppresses the free inversion dynamics between the N–H•••O= and =O •••H–N groups in the ferroelectric 1D column.

Similar doping effects were observed in ferroelectric **4Py**. We prepared chiral (*S*)-**4Py** and its enantiomer (*R*)-**4Py** by introducing chiral (*S*)- or (*R*)-3,7-dimethyloctylamide chains (Fig. 12a).[72,73] Similar to **4Py**, the chiral pyrene derivatives of (*S*)-**4Py** and (*R*)-**4Py** formed 1D molecular assemblies in organic solvents through intermolecular N–H•••O= hydrogen-bonding interaction and exhibited concentration-dependent monomer-excimer emission conversion. This 1D molecular assembly induced a helical 1D configuration of pyrene, and the chiral side chain at the periphery of the molecule induced a helical assembly configuration, resulting in strong circular dichroism (CD) and circular polarized luminescence (CPL) activities. In the CPL spectra in methylcyclohexane, a CPL activity of g_{lum} = 0.03 was obtained for the fluorescence response, which is extremely large for a small molecule. While achiral **4Py** was confirmed to exhibit ferroelectricity in the Col$_h$ liquid crystal phase, (*R*)-**4Py** and (*S*)-**4Py** bearing chiral side chains did not exhibit liquid crystallinity or ferroelectricity, where dipole inversion was suppressed in solids. Therefore, we mixed chiral (*S*)-**4Py** with ferroelectric **4Py** and investigated its molecular assembly structure, phase transition, and ferroelectricity. As in the previous case of mixing antiferroelectric **C14-4BC** with ferroelectric **C14-3BC**, the thermal stability of the Col$_h$ liquid crystal phase was influenced by the doping of the chiral compound into the achiral 1D column. The Col$_h$ liquid crystal phase of **4Py** disappeared completely after approximately 70% mixing with (*S*)-**4Py**, and the mixing of non-liquid crystalline molecules destabilized the Col$_h$ liquid crystal phase. The *T*- and *f*-dependent real part of dielectric constant ε_1 and the *P*-*E* hysteresis curves indicate the ferroelectricity of the (**4Py**)$_{1-x}$((*S*)-**4Py**)$_x$ mixed state. At x = 3%, (*S*)-**4Py** doping causes the disappearance of hysteresis in the *P*-*E* curve (Fig. 12b), which is similar to the result of antiferroelectric **C14-4BC** doping into ferroelectric **C14-3BC**. When chiral (*S*)-**4Py** is randomly introduced into the ferroelectric 1D hydrogen-bonding column of **4Py**, it forms a pinning potential for the inversion motion of the polar amide group, which is the origin of the suppression of ferroelectricity and inhibits macroscopic polarization inversion of the amide group. The column correlation length required for ferroelectricity was estimated to be approximately 12 nm based on the doping amount (Fig. 12c), similar to that found for **C14-4BC** doping into **C14-3BC**. The polarization inversion dynamics of the amide groups in the ferroelectric 1D column was inhibited by slight doping with non-ferroelectric molecules.

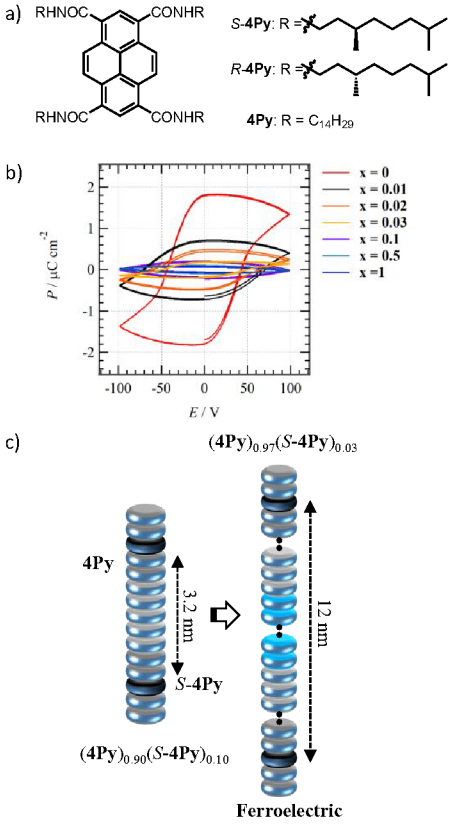

Fig. 12. Control of ferroelectric properties by formation of mixed crystal (**4Py**)$_{1-x}$((*S*)-**4Py**)$_x$. a) Molecular structures of **4Py**, (*S*)-**4Py**, and (*P*)-**4Py**. b) Mixing rate x-dependent *P*-*E* hysteresis curve at f = 0.5 Hz and T = 453 K. c) Mixed state of (**4Py**)$_{1-x}$((*S*)-**4Py**)$_x$ and the correlation length required for the formation of 1D ferroelectricity. Figure modified from ref. 73. Copyright 2019 Wiley-VCH Verlag GmbH & Co. KGaA.

5. Ferroelectricity and low-energy-driven switching of chiral liquid crystalline compounds

The introduction of chirality into the alkylamide chain has a significant effect on the molecular assembly structure and liquid crystallinity, as shown in mixed crystals of (**4Py**)$_{1-x}$((*S*)-**4Py**)$_x$.[73] (*S*)-**3BC** with a chiral (*S*)-3,7-dimethyloctyl group on the alkyl chains of **3BC** derivative was synthesized, and its phase transition behaviour, molecular assembly, and ferroelectricity were compared with those of achiral **C14-3BC** with –CONHC$_{14}$H$_{29}$ chains (Fig. 13a).[74] (*S*)-**3BC** with chiral alkylamide chains exhibited a Col$_h$ liquid crystal phase in the *T*-range of 392–505 K, indicating that the introduction of chirality had no significant effect on the formation of the Col$_h$ liquid crystal phase in the **3BC** system. Scanning electron microscopy

(SEM) images of the organogels formed by (*S*)-**3BC** show the formation of a helical, higher-order molecular assembly structure (Fig. 13b). This corresponds to a helical arrangement of the benzene π-core in the 1D stack via intermolecular N−H•••O= hydrogen bonds due to the introduction of chiral alkyl chains. The *T*- and *f*-dependent real part of dielectric constant ε_1 of (*S*)-**3BC** is similar to that of **C14-3BC**; however, *f*-dependent dielectric peak is characteristic of Debye-type relaxation in the phase transition temperature from the solid to the Col_h liquid crystal phase, a behaviour not observed in the achiral system (Fig. 13c).

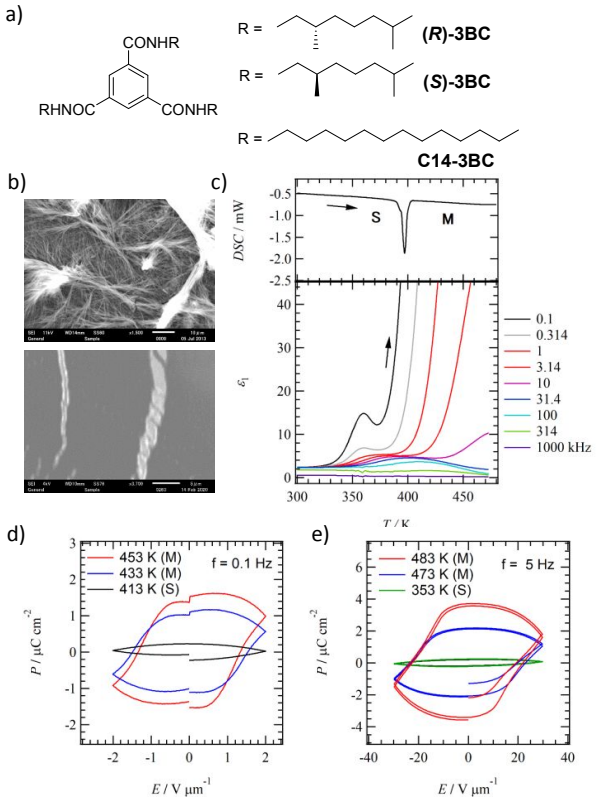

Fig. 13. Dielectric and ferroelectric behaviours of chiral and achiral **3BC** derivatives. a) Molecular structure of **C14-3BC**, (*S*)-**3BC**, and (*R*)-**3BC**. b) SEM images of helical molecular assemblies on HOPG substrate surface (upper scale bar = 10 μm. lower scale bar = 5 μm). c) *T*- and *f*-dependent real part of dielectric constant ε_1 of (*S*)-**3BC**. d) *T*-dependent *P*-*E* hysteresis curve of (*S*)-**3BC** at *f* = 0.1 Hz. e) *T*-dependent *P*-*E* hysteresis curve of *rac*-**3BC** at *f* = 5.0 Hz. Reproduced from ref. 74 with permission from the Royal Society of Chemistry.

In the phase transition from the solid to the Col_h liquid crystal phase, the thermally activated motional freedom associated with the melting of chiral alkyl chains with dipole moments is excited in the Debye-type relaxation. On heating (*S*)-**3BC** in the Col_h liquid crystal phase, a significant ε_1 increase was observed at the low-*f* condition, indicating that the motional freedom of the polar amide groups is thermally activated. Interestingly, a large difference between **C14-3BC** and (*S*)-**3BC** was observed in the measurement of *P*-*E* curves. The P_r and E_t values of (*S*)-**3BC** at 393 K and *f* = 0.5 Hz are 4.5 μC cm^{-2} and 1.7 V μm^{-1}, respectively (Fig. 13d), which are 5.5 times higher and 15 times smaller than the respective P_r and E_t values for **C14-3BC**. The chiral molecular assembly of (*S*)-**3BC** can achieve low energy switching by macroscopic polarization inversion, corresponding to the fact that the inversion energy of the intermolecular N−H•••O= hydrogen bond is reduced to about 1/10 by the introduction of the chiral side chain. The origin of the large difference in E_t values between (*S*)-**3BC** and **C14-3BC** was evaluated from the *T*-dependent asymmetrical N−H stretching vibration mode, which is an index of the strength of intermolecular N−H•••O= hydrogen-bonding interaction. There was no significant difference in the strength of the hydrogen-bonding interactions between (*S*)-**3BC** and **C14-3BC**. In contrast, because (*S*)-**3BC** and **C14-3BC** have different alkyl chain lengths, it is necessary to directly compare (*S*)-**3BC** and *rac*-**3BC**, which were obtained by a 1:1 mixture of *R*-**3BC** and *S*-**3BC**.

6. Uni-directional rotation in ferroelectric liquid crystal phase

The (*S*)- and (*R*)-3,7-dimethyloctylamide chains were used as chiral structural units introduced into **3BC** derivatives, and (*S*)-**3BC** and (*R*)-**3BC** molecules with the same side chain lengths were synthesized to compare the molecular assemblies and ferroelectricity. Because (*S*)-**3BC**, (*R*)-**3BC**, and *rac*-**3BC** have equivalent alkyl chain lengths and molecular weights, the chirality effect can be discussed by comparing their phase transition behaviour and molecular assembly structures (Fig. 13a).[75] In fact, (*R*)-**3BC**, (*S*)-**3BC**, and *rac*-**3BC** show similar phase transition behaviour in DSC charts, and the formation of the Col_h liquid crystal phase is also confirmed by *T*-variable XRD measurements. In contrast, there are two possible mixing modes of *rac*-**3BC**. Each (*R*)-**3BC** or (*S*)-**3BC** forms independent 1D columns, while (*R*)-**3BC** and (*S*)-**3BC** are alternately arranged in a 1D column to form an −*R*−*S*−*R*−*S*−*R*− array in a 1D columnar structure (Fig. 14a). The XRD patterns of these two mixed states in the Col_h liquid crystal phase show a slight difference in the low-angle (100) reflection peaks of the Col_h liquid crystal phase between (*R*)-**3BC** and *rac*-**3BC**. Therefore, the columnar structure in which (*R*)-**3BC** and (*S*)-**3BC** are alternately stacked in a 1D column is a plausible 1D arrangement. Next, we measured the *T*- and *f*-dependent real part of dielectric constant ε_1 of (*R*)-**3BC** and *rac*-**3BC** and observed marked low-*f* enhancement with increasing *T* after the phase transition to the Col_h liquid crystal phase. The measurement of the *P*-*E* curve at 343 K in the Col_h liquid crystal phase shows E_t value of about 1.71 V μm^{-1} for (*R*)-**3BC**, while that of achiral *rac*-**3BC** derivative increases significantly to 23.1 V μm^{-1}. Therefore, E_t value of chiral (*R*)-**3BC** is approximately 20 times lower than that of achiral *rac*-**3BC** (Figs. 13d, e). In contrast, the P_r value of (*R*)-**3BC** is approximately two times larger than that of *rac*-**3BC**.

The reason for the large difference in *P*-*E* hysteresis curve is discussed in the ferroelectric states of (*R*)-**3BC** and *rac*-**3BC**. The E_t values of (*R*)-**3BC** and *rac*-**3BC** were determined at 1.71 and 23.1 V μm^{-1}, respectively, and the *f*-responses of the *P*-*E* hysteresis curves of (*R*)-**3BC** and *rac*-**3BC** were clearly observed

at 0.1 and 5.0 Hz, respectively. Furthermore, the *T*- and *f*-dependent real part of dielectric constant ε_1 shows a larger response for *rac*-**3BC** than for (*R*)-**3BC**. Based on these results, the following polarization inversion mechanism was postulated: In *rac*-**3BC**, (*R*)-**3BC** and (*S*)-**3BC** form alternative stacks of 1D columns, and the polarization inversion dynamics of the polar N−H•••O= amide group are considered to be either random or alternating right and left rotations (Fig. 14b). In contrast, the rotational direction of the polar amide group in chiral (*R*)-**3BC** is restricted owing to steric hindrance caused by the chirality of the side alkyl chain, resulting in unidirectional rotational dynamics. In other words, polarization inversion of the polar amide group by right- or left-handed rotational motion occurs depending on molecular chirality. The existence of unidirectional rotational dynamics is similar to the rotational mode realized in biological molecular motors such as ATPase and is a requirement for a motor to perform actual work. These unidirectional dipole inversion dynamics are thought to greatly reduce the energy of E_t required for polarization inversion. Controlling rotational motion by introducing chiral alkylamide chains is an important technique for fabricating memory devices with the low-energy-consumption feature, and chiral organic ferroelectrics are interesting targets for the realization of molecular electronic devices.

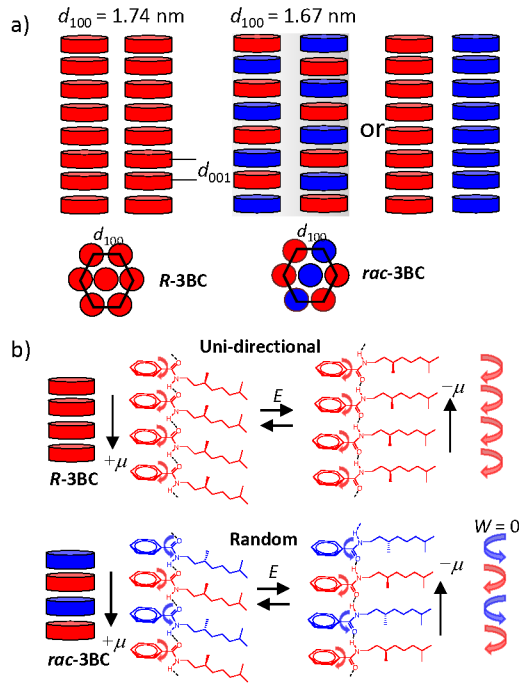

Fig. 14. Molecular assembly structure of (*R*)-**3BC** and *rac*-**3BC** and their motional freedom. a) Columnar structure of (*R*)-**3BC** and *rac*-**3BC** estimated from *T*-variable XRD patterns of Col_h phase. b) Unidirectional rotational motion of amide groups in (*R*)-**3BC** and alternate random rotational motion in *rac*-**3BC**. Adapted with permission from ref. 75. Copyright 2022 American Chemical Society.

7. Dynamic alkylamide group and ferroelectricity in the solid state

In the Col_h liquid crystal phase, the alkyl chains were sufficiently melted like in the liquid state through thermal fluctuations, where the inversion motion of the polar amide groups was relatively easily realized to demonstrate ferroelectricity accompanied by polarization inversion motion of N−H•••O= groups. In contrast, the **2BC** derivative of **C14-TPA**, in which the $-CONHC_{14}H_{29}$ chains are substituted at the para-position of benzene, has been shown to exhibit ferroelectric behaviour with a *P*-*E* hysteresis curve,[66] even though it does not exhibit the Col_h liquid crystal phase. The very simple molecular structure of **Cn-TPA** derivatives exhibits a successive solid-solid phase transition depending on the alkyl chain length (n), and ferroelectricity is detected in derivatives with longer alkyl chain lengths (n > 10).[76]

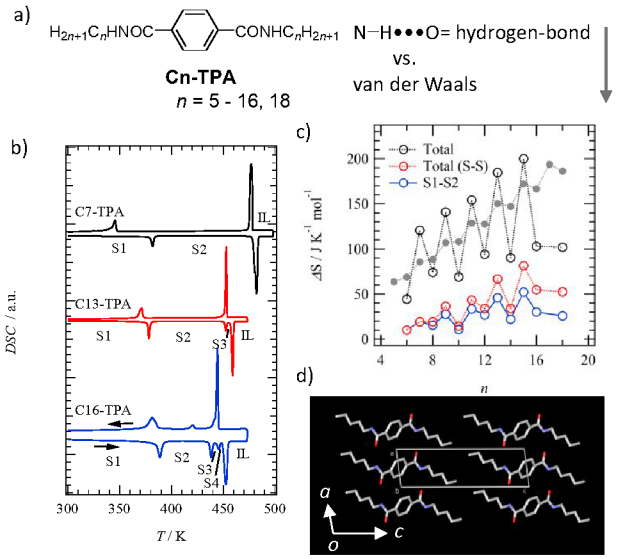

Fig. 15. Molecular assembly structure of **Cn-TPA**. a) Molecular structure of **Cn-TPA** and control of intermolecular interaction by alkyl chain length n. b) DSC charts of **C7-TPA**, **C13-TPA**, and **C16-TPA**, and existence of successive solid-solid phase transitions. c) n-dependent transition entropy change (Δ*S*). d) Unit cell of **C5-TPA** viewed along the *b*-axis based on single-crystal X-ray structural analysis (CCDC-2110544). Reproduced from ref. 76 with permission from the Royal Society of Chemistry.

The inversion dynamics of intermolecular N−H•••O= hydrogen bonds are observed in thermally fluctuating flexible molecular assemblies such as the Col_h liquid crystal phase. Systematically varying the alkyl chain length from n = 5 to n = 18 in **Cn-TPA** derivatives adjusts the balance between the hydrogen-bonding interaction of the N−H•••O= group and the van der Waals interaction of the alkyl chain (Fig. 15). We investigated the phase transition behaviour and ferroelectricity of a series of **Cn-TPA** derivatives with controlled alkyl-chain lengths. All the **Cn-TPA** derivatives showed successive solid-solid phase transitions as *T* increased from room temperature, and the number of solid-solid phase transitions increased with the much longer chain length (Fig. 15b). The phase transition entropy change (Δ*S*) showed an even-odd effect, with the Δ*S* values being lower in the even-numbered alkyl chain derivatives than in the odd-numbered derivatives (Fig. 15c). To clarify the molecular assembly structure of the **Cn-TPA** derivatives, single-crystal X-ray structure analysis of **C5-TPA** was successfully

conducted. Fig. 15d shows the 1D molecular assembly structure of **C5-TPA**. The 1D molecular assembly structure was also confirmed by the SEM images of spin-coated films fabricated on the highly ordered pyrolytic graphite (HOPG) substrate surface, showing the growth of whisker-like crystals. The molecular assembly structures and their changes in each solid phase were evaluated by variable-*T* XRD measurements. The lamellar structure formed by intermolecular N–H•••O= hydrogen-bonding interaction was retained in all solid phases; however, the reflection around 2θ~20° broadened with increasing *T*, indicating that the thermal motion of alkyl chains is activated in the high-*T* crystalline phase. The alkyl chains have a high degree of freedom of thermal motion, despite being in the solid phase.

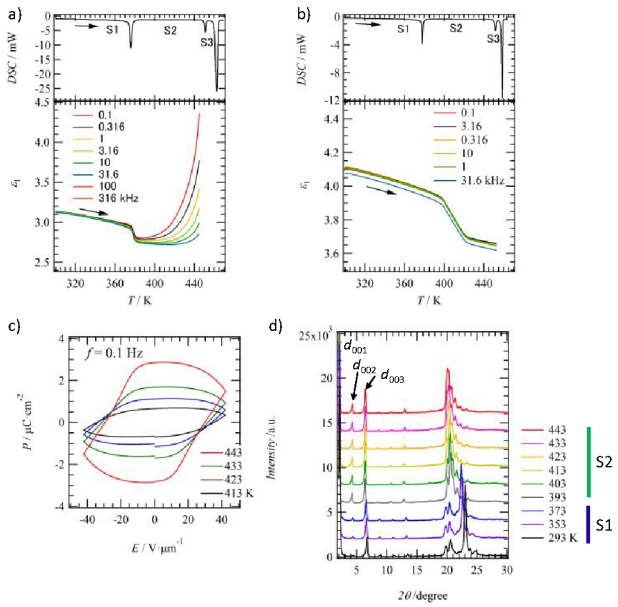

Fig. 16. Dielectric behaviour, ferroelectricity, and molecular assembly of **Cn-TPA** derivatives. *T*- and *f*- dependent real part of dielectric constants ε_1 for a) **C12-TPA** and b) **C13-TPA** with the corresponding DSC charts. c) *T*-dependent *P*-*E* curve of **C15-TPA** at *f* = 0.1 Hz. d) *T*-variable XRD pattern of **C13-TPA**. Reproduced from ref. 76 with permission from the Royal Society of Chemistry.

Figs. 16a, b show the *T*- and *f*-dependent real part of dielectric constant ε_1 of even-chain **C12-TPA** and odd-chain **C13-TPA**, respectively. An increase in dielectric constant ε_1 in the low-*f* region with increasing *T* is observed for the even-chain **Cn-TPA** derivative (Fig. 16a), suggesting that the high-*T* (S2 and S3) phases are thermally fluctuating molecular assembly structures similar to liquid crystalline phases. However, dielectric anomalies of the odd-chain **C13-TPA** were accompanied by *f*-independent behaviour with increasing *T* after the phase transition from S2 to S3, although the *f*-dependence in dielectric constants was observed in even-chain **C12-TPA** (Figs. 16a, b). The *T*-dependent real part of dielectric constant ε_1 depends on the alkyl chain length, and a large difference was observed between the odd and even chains. This suggests that there are differences in the molecular assembly structure and the thermal dynamics of the polar N–H•••O= hydrogen-bonding interaction between the odd and even chains system of **Cn-TPA**. The *f*-response of dielectric constants of even-numbered chains is larger than that of odd-numbered chains. The *P*-*E* hysteresis curve was observed in **Cn-TPA** derivatives with chain lengths longer than n = 11 (Fig. 16c). *T*-variable XRD patterns of the high-*T* crystalline phase of the longer chain **Cn-TPA** derivative showed a broadening of the reflection peaks around 2θ ~ 20° (Fig. 16d), indicating that the two alkylamide chains were partially melted by thermal motion at the high-*T* solid phase. Correspondingly, the thermal motion of the polar amide groups was activated, and ferroelectricity appeared in the solid phase due to the polarization inversion dynamics.

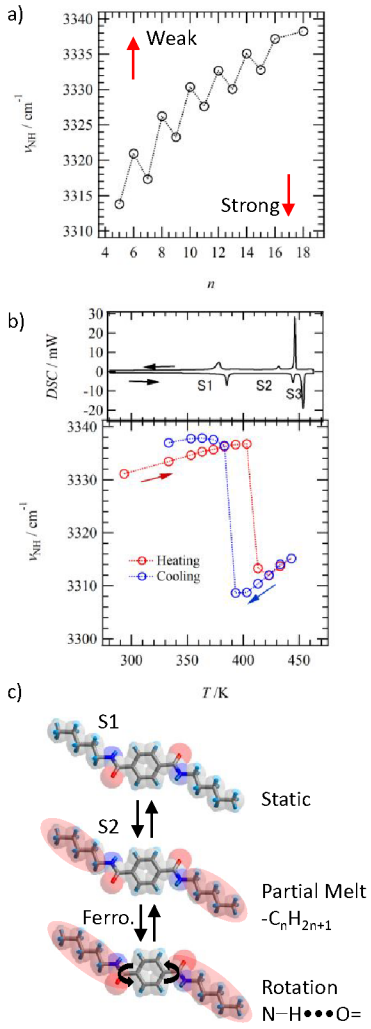

Fig. 17. Mechanisms of conformational changes and ferroelectricity in **Cn-TPA**. a) Alkyl chain length dependent N–H symmetrical stretching vibrational modes (ν_{NH}) corresponding to intermolecular amide-type hydrogen-bonding interaction. b) *T*-dependent ν_{NH} energy of **C15-TPA** and corresponding DSC charts. c) Thermal excitation processes of partial alkyl chain melting and rotational motion of intermolecular amide groups in phase transitions of **Cn-TPA**. Reproduced from ref. 76 with permission from the Royal Society of Chemistry.

The strength of the intermolecular N–H•••O= hydrogen-bonding interaction was evaluated using *T*-variable infrared (IR) spectroscopy. The strength of the intermolecular hydrogen bonds of the amide groups with respect to the alkyl chain length revealed a blue shift in the N–H asymmetrical stretching

vibration mode (ν_{NH}) with increasing chain length n, and the hydrogen-bonding interaction became weaker (Fig. 17a). Furthermore, the ν_{NH} of the amide group showed a phase transition from the low-*T* solid (S1) to the high-*T* phase (S2 and S3), which supported the partial melting of the alkyl chain accompanied by a discontinuous change in the intermolecular N−H•••O= hydrogen-bonding interactions (Fig. 17b).

These results suggest that **Cn-TPA** exists in a static crystalline state in the low-*T* solid phase, and transforms to the high-*T* dynamic solid phase in the S2 or S3 states with increasing *T*. In the S2 and S3 states, the alkyl chains are partially melted to form flexible molecular assemblies that can undergo polarization inversion upon the application of an external electric field. A liquid crystalline state does not necessarily demonstrate ferroelectricity, and thermal fluctuations of alkyl chains similar to the liquid crystalline state can be realized even in the solid state by introducing long alkyl chains of appropriate length. In the liquid crystalline phase, a relaxation process of the polarization state is observed over time, whereas this relaxation process is considered slow in the solid phase. However, compared to common crystalline ferroelectrics, the ferroelectricity of the present **Cn-TPAs** is accompanied by partial thermal melting of the alkyl chains, similar to the liquid crystal state; thus, the polarization relaxation process is considered relatively fast. Recently, ferroelectricity in plastic crystalline phases has been reported. In such systems, dipole inversion dynamics are possible while maintaining the molecular center of gravity, increasing the material design of organic ferroelectrics.[77–85] Soft molecular assemblies such as liquid crystals and plastic crystals are considered suitable systems for the control of physical properties using molecular dynamics.

8. Summary

This review describes the previous research from the author's group, focusing on alkylamide chains from the viewpoint of chemical design of ferroelectricity. The stabilization of the Col_h liquid crystal phase using alkylamide chains proposed by Matsunaga provides an important structural unit for the design of molecular assembly structures, especially for the formation of low-dimensional molecular assembly structures such as supramolecular polymers. Furthermore, the alkylamide chain evolves into a structural unit that plays an important role in the design of ferroelectric molecular assemblies as a dynamic structural unit that enables polarization inversion in the liquid crystal and solid phases. The appropriate strength of intermolecular hydrogen bonds can invert the direction of polarization by the application of an external electric field, and thermal fluctuations of long alkylamide chains are effective as flexible and dynamic structural units to realize a ferroelectric response. Alkylamide chains can be conventionally combined with various π-electron frameworks to design a variety of functional molecular assemblies. The introduction of chirality into alkylamide chains enables the control of ferroelectricity and molecular rotation dynamics, providing an important molecular design principle for next-generation ferroelectric memory and molecular machines. In contrast, various functional π-cores such as pyrene and porphyrin can be designed as the π-electron backbone, enabling the addition of various functions such as luminescence and high thermal stability to ferroelectricity. For instance, ferroelectrics with conductive π-electron cores can be fabricated, enabling the fabrication of novel multifunctional materials with coexisting conductivity and ferroelectricity, which are typically mutually contradictory properties. This approach to the fabrication of multifunctional molecular materials is a useful chemical technique based on the exploration of physical properties with a focus on dynamic molecular assemblies and will become important in the future to realize next-generation molecular machines. The control of the dynamics in molecular assemblies is a guiding principle that can be applied to realize a wide variety of functional materials. The development of molecular systems for the study of dynamic molecular systems has become a feature material target.

Conflicts of interest

There are no conflicts to declare.

Acknowledgements

We are very grateful to Prof. Yoshio Matsunaga (Emeritus Professor of Hokkaido University), Prof. Gunzi Saito (Emeritus Professor of Kyoto University), and Prof. Takayoshi Nakamura (Hokkaido University) for their help in preparing this review. This work was carried out by students working under Prof. Akutagawa (2010–present) and other collaborators. Research funding included a Grant-in-Aid for Transformative Research Areas (A) "Condensed Conjugation" (JP20H05865), Japan; KAKENHI (JP19H00886, JP20H04655, and JP20K05442) from MEXT; JST CREST Grant Number JPMJCR18I4; and 'Dynamic Alliance for Open Innovation Bridging Human, Environment, and Materials' from MEXT.

Notes and references

1 *Advances in Protein Chemistry Vol. 72, Peptide Solvation and H-Bonds*, R. L. Baldwin, D. Baker, eds.; Elsevier Academic Press: Amsterdam, 2006.
2 *The Amide Linkage*, A. Greenberg, C. M. Breneman, J. F. Liebman, eds.; Wiley-Interscience: New Jersey, 2003.
3 T. Akutagawa, *Mater. Chem. Front*. 2018, **2**, 1064–1073.
4 T. Akutagawa, *Bull. Chem. Soc. Jpn*. 2021, **94**, 1400–1420.
5 T. Akutagawa, T. Takeda, N. Hoshino, *Chem. Comm*. 2021, **57**, 8378–8401.
6 M. L. Bushey, T. -Q Nguyen, W. Zhang, D. Horoszewski, C. Nuckolls, *Angew. Chem. Int. Ed*. 2004, **43**, 5446–5453.
7 B. Roy, T. Govindaraju, *Bull. Chem. Soc. Jpn*. 2019, **92**, 1883–1901.
8 T. F. A. De Greef, M. M. J. Smulders, M. Wolffs, A. P. H. J. Schenning, R. P. Sijbesma, E. W. Meijer, *Chem. Rev*. 2009, **109**, 5687–5754.
9 A. Sharko, D. Livitz, S. De Piccoli, K. J. M. Bishop, T. M. Hermans, *Chem. Rev*. 2022, **122**, 11759–11777.
10 S. Chandrasekhar, B. K. Sadashiva, K. A. Suresh, Pramana 1977, **9**, 471–480.

11 S. Kumar, Chemistry of Discotic Liquid Crystals, CRC Press, N.Y., 2011.
12 Y. Geng, A. Fechtenkötter, K. Müllen, *J. Mater. Chem.* 2001, **11**, 1634−1641.
13 S. Kumar, S. Setia, B. S. Avinash, *Liq. Cryst.,* 2013, **40**, 1769−1816.
14 Y. Matsunaga,Y. Nakayasu, S. Sakai, M. Yonenaga, *Mol. Cryst. Liq. Cryst*. 1986, **141**, 327−333.
15 Y. Matsunaga, N. Miyajima, Y. Nakayasu, S. Sakamoto, M. Yonenaga, *Bull. Chem. Soc. Jpn*. 1988, **61**, 207−210.
16 Y. Kobayashi, Y. Matsunaga, *Bull. Chem. Soc. Jpn*. 1987, **60**, 3515−3518.
17 Y. Harada, Y. Matsunaga, N. Miyajima, S. Sakamoto, *J. Mater. Chem*., 1995, **5**, 2305−2308.
18 H. Kawada, Y. Matsunaga, T. Takamura, M. Terada, *Can. J. Chem*. 1988, **66**, 1867−1871.
19 H. Kawada, Y. Matsunaga, *Bull. Chem. Soc. Jpn*., 1988, **61**, 3083−3085.
20 H. Kawada, Y. Matsunaga, *Bull. Chem. Soc. Jpn*., 1990, **63**, 1691−1694.
21 J. Kawamata, Y. Matsunaga, *Mol. Cryst. Liq. Cryst*., 1993, **231**, 79−85.
22 T. Akutagawa , K. Iuchi, Y. Matsunaga, *Liq. Cryst*., 1997, **27**, 1399−1403.
23 P. Terech, R. G. Weiss, *Chem. Rev*. 1997, **97**, 3313-3362.
24 Y. Ohsedo, H. Watanabe, M. Oono, A. Tanaka, *RSC Adv*., 2013, **3**, 5803–580.
25 V. A. Mallia, M. George, D. L. Blair and R. G. Weiss, *Langmuir*, 2009, **25**, 8615–8625.
26 Y. Yasuda, E. Ishii, H. Inada, Y. Shirota, *Chem. Lett*., 1996, **1996**, 575−576.
27 K. Hanabusa, C. Koto, M. Kimura, H. Shirai, A. Kakehi, *Chem. Lett*., 1997, **1997**, 429−430.
28 J. Malthête, A. –M. Levelut, L. LiPbert, *Adv. Mater*., 1992, **4**, 37−41.
29 J. S. Moore, *Curr. Opin. Coll. Inter. Sci*. 1999, **4**, 108−116.
30 L. Brunsveld, B. J. B. Folmer, E. W. Meijer, R. P. Sijbesma, *Chem. Rev*., 2001, **101**, 4071–4098.
31 T. Aiada. W. Meijer, S. I. Stupp, *Science*, 2012, **335**, 813−817.
32 A. Das, G. Vantomme, A. J. Markvoort, H. M. M. ten Eikelder, M. Garcia-Iglesias, A. R. A. Palmans, E. W. Meijer, *J. Am. Chem. Soc*., 2017, **139**, 7036−7044.
33 S. Cantekin, H. M. M. ten Eikelder, A. J. Markvoort, M. A. J. Veld, P. A. Korevaar, M. M. Green, A. R. A. Palmans, E. W. Meijer, *Angew. Chem. Int. Ed*., 2012, **51**, 6426−6431.
34 H. M. M. ten Eikelder, A. J. Markvoort, T. F. A. de Greef, P. A. J. Hilbers, *J. Phys. Chem. B*, 2012, **116**, 5291−5301.
35 A. J. Markvoort, H. M. M. ten Eikelder, P. A. J. Hilbers, T.F. A. de Greef, E. W. Meijer, *Nat. Comm*., 2011, **2**, 509−1−9.
36 P. J. M. Stals, M. M. J. Smulders, R. Martin-Rapun, A. R. A. Palmans, E. W. Meijer, *Chem. Eur. J*., 2009, **15**, 2071−2080.
37 M. M. J. Smulders, A. P. H. J. Schenning, E. W. Meijer, *J. Am. Chem. Soc*., 2008, **130**, 606−611.
38 A. J. Wilson, M. Masuda, R. P. J. Sijbesma, E. W. Meijer, *Angew. Chem. Int*., 2005, **44**, 2275−2279.
39 J. J. van Gorp, J. A. J. M. Vekemans, E, W, Meijer, *J. Am. Chem. Soc*., 2002, **124**, 14759−14769.
40 M. Wegner, D. Dudenko, D. Sebastiani, A. R. A. Palmans, T. F. A. de Greef, R. Graf, H. W. Spiess, *Chem. Sci*., 2011, **2**, 2040−2049.
41 M. M. J. Smulders, P. J. M. Stals, T. Mes, T. F. E. Paffen, A. P. H. J. Schenning, A. R. A. Palmans, E. W. Meijer, *J. Am. Chem. Soc*., 2010, **132**, 620−626.
42 M. M. J. Smulders, I. A. W. Filot, J. M. A. Leenders, P. van der Schoot, A. R. A. Palmans, A. Ph. H. J. Schenning, E. W. Meijer, *J. Am. Chem. Soc*., 2010, **132**, 611−619.
43 S. Ogi, V. Stepanenko, K. Sugiyasu, M. Takeuchi, F. Würthner, *J. Am. Chem. Soc*. 2015, **137**, 3300–3307.
44 T. Fukui, S. Kawai, S. Fujinuma, Y. Matsushita, T. Yasuda, T. Sakurai, S. Seki, M. Takeuchi, K. Sugiyasu, *Nat. Chem*., 2017, **9**, 493–1–9.
45 T. Fukui, N. Sasaki, M. Takeuchi, K. Sugiyasu, *Chem. Sci*., 2019, **10**, 6770−6776.
46 T. Miyashita, Y. Mizuta, M. Matsuda, *Poly. Int*. 1990, **22**, 327−331.
47 Y. Mizuta, M. Matsuda, T. Miyashita, *Langmuir* 1993, **9**, 1158−1159.
48 A. S. Tayi, A. Kaeser, M. Matsumoto, T. Aida, and S. I. Stupp, *Nat. Chem*., 2015, **7**, 281–294.
49 S. Horiuchi and Y. Tokura, *Nat. Mater*., 2008, **7**, 357–366.
50 S. Horiuchi, Y. Tokunaga, G. Giovannetti, S. Picozzi, H. Itoh, R. Shimano, R. Kumai, Y. Tokura, *Nature* 2010, **463**, 789–792.
51 B. Stadlober, M. Zirkl and M. Irimia-Vladu, *Chem. Soc. Rev*., 2019, **48**, 1787–1825.
52 K. Kishikawa, S. Nakahara, Y. Nishikawa, S. Kohmoto, M. Yamamoto, *J. Am. Chem. Soc*., 2005, **127**, 2565–2571.
53 D. Miyajima, F. Araoka, H. Takezoe, J. Kim, K. Kato, M. Takata and T. Aida, *Science*, 2012, **336**, 209–213.
54 J. F. Stoddart and S. I. Stupp, *J. Am. Chem. Soc*., 2017, **139**, 9186–9199.
55 T. Akutagawa, H. Koshinaka, D. Sato, S. Takeda, S. Noro, H. Takahasi, R. Kumai, Y. Tokura, T. Nakamura, *Nat. Mater*., 2009, **8**, 342–347.
56 J. Ichikawa, N. Hoshino, T. Takeda, T. Akutagawa, *J. Am. Chem. Soc*. 2015, **137**, 13155−13160.
57 D. Asthana, A. Kumar, A. Pathak, P. K. Sukul, S. Malik, R. Chatterjee, S. Patnaik, K. Rissanene, P. Mukhopadhyay, *Chem. Comm*. 2011, **47**, 8928–8930.
58 C. F. C. Fitié, W. S. C. Roelofs, M. Kemerink, R. P. Sijbesma, *J. Am. Chem. Soc*., 2010, **132**, 6892−6893.
59 Fitié, C. F. C.; Roelofs, W. S. C.; Magusin, P. C. M. M.; Wübbenhorst, M.; Kemerink, M.; Sijbesma, R. P. *J. Phys. Chem. B*, 2012, **116**, 3928– 3937.
60 C. F. C. Fitié, I. Tomatsu, D. Byelov,W. H. de Jeu, R. P. Sijbesma, *Chem. Mater*., 2008, **20**, 2394−2404.
61 I. Urbanaviciute, X. Meng, T. D. Cornelissen, A. V. Gorbunov, S. Bhattacharjee, R. P. Sijbesma, M. Kemerink, *Adv. Electron. Mater*., 2017, **3**, 1600530−1−7.
62 A. V. Gorbunov, T. Putzeys, I. Urbanavičiūtė, R. A. J. Janssen, M. Wübbenhorst, R. P. Sijbesma, M. Kemerink, *Phys. Chem. Chem. Phys*., 2016, **18**, 23663−23672.
63 D. Mandal, R. K. Roy, A. Mukherjee, S. Barman, A. Ghosh, S. Chakraborty, A. Datta, A. Datta, S. Ghosh, *Chem. Sci*., 2022, **13**, 781−788.
64 C. Park, K. Lee, M. Koo, C. Park, *Adv. Mater*., 2020, **33**, e2004999-1-28.
65 K. C. Kao, *Dielectric Phenomena in Solids*, Elsevier, Amsterdam, 2004.
66 Y. Shishido, H. Anetai, T. Takeda, N. Hoshino, S. -i. Noro, T. Nakamura, T. Akutagawa, *J. Phys. Chem. C*, 2014, **118**, 21204−21214.
67 H. Anetai, Y. Wada, T. Takeda, N. Hoshino, S. Yamamoto, M. Mitsuishi, T. Takenobu, T. Akutagawa, *J. Phys. Chem. Lett*., 2015, **6**, 1813−1818.
68 J. Wu, T. Takeda, N. Hoshino, Y. Suzuki, J. Kawamata, T. Akutagawa, *J. Phys. Chem. C*, 2019, **123**, 22439−22446.
69 J. Wu, Q. Zhu, T. Takeda, N. Hoshino, T. Akutagawa, *ACS Appl. Electron. Mater*., 2021, **3**, 3521−3529.
70 H. Anetai, T. Takeda, N. Hoshino, H. Kobayashi, N. Saito, M. Shigeno, M. Yamaguchi, T. Akutagawa, *J. Am. Chem. Soc*., 2019, **141**, 2391−2397.
71 J. Wu, T. Takeda, N. Hoshino, T. Akutagawa, *J. Phys. Chem. B*, 2020, **124**, 7067–7074.
72 H. Anetai, T. Takeda, N. Hoshino, Y. Araki, T. Wada, S. Yamamoto, M. Mitsuishi, H. Tsuchida, T. Ogoshi, T. Akutagawa, *J. Phys. Chem. C*, 2018, **122**, 6323–6331.

73 H. Anetai, K. Sambe, T. Takeda, N. Hoshino, T. Akutagawa, *Chem. Eur. J*. 2019, **25**, 11233–11239.
74 J. Wu, T. Takeda, N. Hoshino, T. Akutagawa, *J. Mater. Chem. C*, 2020, **8**, 10283–10289.
75 J. Wu, T. Takeda, N. Hoshino, T. Akutagawa, *J. Phys. Chem. C*, 2022, **126**, 3864–3871.
76 M. Kawana, R. Mizoue, T. Takeda, N. Hoshino, T. Akutagawa, *J. Mater. Chem. C*, 2022, **10**, 4208–4217.
77 J. Harada, T. Shimojo, H. Oyamaguchi, H. Hasegawa, Y. Takahashi, K. Satomi, Y. Suzuki, J. Kawamata, T. Inabe, *Nat. Chem*., 2016, **8**, 946–1–7.
78 J. Harada, N. Yoneyama, S. Yokokura, Y. Takahashi, A. Miura, N. Kitamura, T. Inabe, *J. Am. Chem. Soc*., 2018, **140**, 346–354.
79 P.-P. Shi, Y. -Y. Tang, P. -E. Li, W. -Q. Liao, Z. -X. Wang, Q. Ye, R. -G. Xiong, *Chem. Soc. Rev*., 2016, **45**, 3811– 3827.
80 P. –E. Li, Y.-Y. Tang, Z.-X. Wang, H.-Y. Ye, Y.-M. You, R.-G. Xiong, *Nat. Commun*. 2016, **7**, 13635–1–7.
81 H.-Y. Ye, J.-Z. Ge, Y.-Y. Tang, P.-F. Li, Y. Zhang, Y.-M. You, R.-G.; Xiong, *J. Am. Chem. Soc*. 2016, **138**, 13175–13178.
82 Y.-Y. Tang, W.-Y. Zhang, P.-F. Li, H.-Y. Ye, Y.-M. You, R.-G. Xiong, *J. Am. Chem. Soc*. 2016, **138**, 15784–15789.
83 Y.–M. You, Y.-Y. Tang, P.-F. Li, H.-Y. Zhang, W.-Y. Zhang, Y. Zhang, H.-Y Ye, T. Nakamura, R.-G. Xiong, *Nat. Commun*. 2017, **8**, 14934–1–7.
84 Q. Pan, Z.-B. Liu, H.-Y. Zhang, W.-Y. Zhang, Y.-Y. Tang, Y.-M. You, P.-F. Li, W.-Q. Liao, P.-P. Shi, R.-W. Ma, R.-Y. Wei, R.-G. Xiong, *Adv. Mater*., 2017, **29**, 1700831–1–7.
85 S. Furukawa, J. Wu, M. Koyama, K. Hayashi, N. Hoshino, M. Saito, T. Akutagawa, *Nat. Commun*., 2021, **12**, 768–1–7.